*J. Fluid Mech.* (2023), *vol*. 975, A51, doi:10.1017/jfm.2023.907

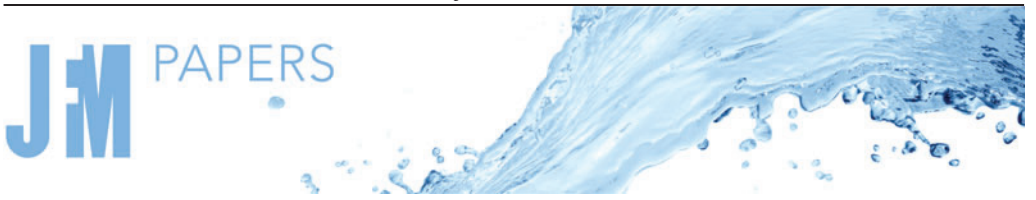


# Dynamic separation on an accelerating prolate spheroid

**Pengming Guo**[1],†, **Frieder Kaiser**[1] **and David E. Rival**[1,2]

[1]Department of Mechanical and Materials Engineering, Queen's University, Kingston, ON K7L 3N6, Canada

[2]Institute of Fluid Mechanics, Technische Universität Braunschweig, Hermann-Blenk-Str. 37, Braunschweig 38106, Germany

(Received 30 May 2023; revised 19 September 2023; accepted 19 October 2023)

Time-varying flow separation on an accelerating prolate spheroid has been studied at various angles of incidence. Instantaneous pressure and scanning stereoscopic particle image velocimetry were used to shed light on the evolution of cross-flow structures for the Reynolds number ($Re$) range of $1.0 \times 10^6 \leq Re \leq 1.5 \times 10^6$. The movement of separation lines is examined for various model accelerations to investigate on the interplay between acceleration and flow separation. The results demonstrate that for axial accelerations, the streamwise pressure distribution in the rear part of the prolate spheroid switches from an adverse to a favourable pressure gradient. At the same time, the circumferential adverse pressure gradient present during steady motion vanishes during said accelerations. In contrast, both streamwise and circumferential adverse pressure gradients strengthen when the model is axially decelerated. These dynamic pressure distributions influence the location of the separation line, which in turn moves closer to the model meridian during accelerations while moving outwards during decelerations. The streamwise vorticity distribution and the streamwise circulation both show how the separation-line position impacts the vortex formation. A high-vorticity region near the model surface is established during acceleration. In contrast, a decelerating model leads to transport of high-vorticity fluid into the outer area of the cross-flow separation. We further assess the memory effects following the near-impulsive velocity changes. The cross-flow retains the memory of moving separation lines shortly after the acceleration. However, the separation recovers quickly to a steady state.

**Key words:** flow–structure interactions, separated flows, vortex dynamics

† Email address for correspondence: pengming.guo@queensu.ca

## 1. Introduction

Unsteady three-dimensional (3-D) flow separation is a ubiquitous phenomenon that can be observed in flows both in nature as well as in engineering. Examples include the swimming of fish (Zhang *et al.* 2022), birds and aircraft experiencing gusts (Cheney *et al.* 2020), or even rapid submarine manoeuvring (Bettle, Gerber & Watt 2009). To-date, many studies on unsteady flow separation have focused on two-dimensional (2-D) flow separation (Yu *et al.* 2018; Li *et al.* 2020; Miotto *et al.* 2022). With regards to 3-D separation, most studies have restricted themselves to investigations of complex separation mechanics with steady boundary conditions. One common canonical test case is that of the 6:1 prolate spheroid due to the abundance of complex flow features that occur even at small incidence angles. The transition of the boundary layer to turbulence (Wetzel 1996), pressure-gradient induced separations (El Khoury, Andersson & Pettersen 2012) and helical vortex formations (Jiang *et al.* 2016) are but a few phenomena that have been extensively studied using the prolate-spheroid geometry. However, for highly unsteady, 3-D separating flows, a limited amount of studies exist. As such, many aspects of dynamic 3-D flow separation processes have not been explored. For instance, how the 3-D separated flow around a prolate spheroid reacts to a sudden change in boundary conditions has not yet been considered. To gain a deeper understanding of how unsteadiness affects separating 3-D flows, we use the well-characterized 6:1 prolate spheroid and investigate how the separated wake and the surface pressure distribution are influenced by acceleration and deceleration.

### 1.1. *Background on flow separation*

Flow separation has often been categorized into two categories: separation due to an abrupt change of the geometry and detachment on flat (or mildly curved) surfaces owing to the existence of a strong adverse pressure gradient (APG) (Deck 2012). The former category is characterized by its fixed separation location. Classical examples include the backward-facing step (Le, Moin & Kim 1997), splitter plate (Hwang, Yang & Sun 2003) or an inclined flat plate (Stevenson, Nolan & Walsh 2016). In contrast, the separation induced by an APG on a smooth surface is relatively complex due to its intermittent behaviour; the locations of separation and reattachment vary due to disturbances in the pressure-gradient field (Simpson, Chew & Shivaprasad 1981). The flow within a diffuser (Elyasi & Ghaemi 2019), the flow around an airfoil (Ma, Gibeau & Ghaemi 2020) or the flow around a prolate spheroid (Jiang *et al.* 2016) all belong to the above category.

For smooth geometries with intermittent separation (APG induced), the definition of the separation location depends on whether the flow is two-dimensional or three-dimensional in nature. For 2-D flow separation, Prandtl (1904) derived a criterion based on the no-slip boundary condition, implying that the flow separates at a point with zero wall shear and the skin friction admits a negative gradient. For unsteady boundary conditions, the separation point may move (Rott 1956; Moore 1958; Sears & Telionis 1971; Haller 2004). More recently, Lamarche-Gagnon & Vétel (2018) observed the moving separation point in a rotor-oscillator flow using a cylinder in non-periodic transitions.

In 3-D flows, however, separation occurs along lines, and not at points of zero skin-friction (Tobak & Peake 1982; Simpson 1995; Délery 2001). After the first studies on 3-D separation published by Legendre (1952), a heuristic 3-D flow separation criterion was then proposed by Lighthill (1963), who hypothesized that separation lines originate from regions of zero skin friction and that the separation line must be a closed curve. Wang (1972, 1974) listed some examples where Lighthill's rule does not apply and where

the separation line and zero skin-friction regions do not coincide. Wang (1976) further distinguishes between open and closed separation. For a closed separation, the separation line is closed upstream of the separation, preventing the upstream flow entering the separated area; see for example figure 1(*a*). In contrast, for an open separation, the limiting streamlines run directly into the separated region; see figure 1(*b*). More detailed criteria of steady 3-D flow separation were derived by Wu *et al.* (2000), Wu, Ma & Zhou (2007) and Surana, Grunberg & Haller (2006). These studies clearly distinguish between open and closed separation zones. Four possible separation line signatures are thus summarized: saddle nodes; saddle-limit cycles; saddle spirals and limit cycles (Surana *et al.* 2006).

### 1.2. *Examples of unsteady 3-D flow separation*

A simple example of unsteady 3-D separation occurs for the flow around a sphere, as illustrated in figure 1(*c*). Owing to the axisymmetry of the problem, the flow shows very similar features to that of the 2-D problem of the flow separation around a cylinder. Under subcritical conditions, Fernando *et al.* (2017) confirmed that the separation line on a sphere moves downstream during acceleration, which is consistent with the moving characteristic of the APG-induced flow separation observed for 2-D problems. The phenomenon of moving separation lines was explained via theoretical considerations based on the unsteady potential-flow solution around an accelerating sphere. Specifically, in unsteady potential flow, the pressure-gradient field around a sphere shifts from adverse to favourable for strong accelerations.

Moving on to fully 3-D separated flows, the flow over delta wings has been widely studied (Gursul 2005). On a delta wing at high incidence angles, two large, counter-rotating vortices roll up from the leading edges (separation lines) on the wing suction side. Note that the separation line lies very close to the wing apex for a thick delta wing with rounded leading edges (Délery 2001). Even in unsteady flows, dynamic motions do not change the location of the separation line on a delta wing significantly (Gursul 2005). However, unsteady kinematics influence other flow features, such as the changing position of the vortex centre and varying locations of vortex breakdown (Lowson & Riley 1995; Délery 2001; Mitchell & Délery 2001). Marzanek & Rival (2019) studied the effects of streamwise acceleration on the flow around a non-slender delta wing at various incidence angles. Although the separation line was fixed, as sketched in figure 1(*d*), the separated flow would reattach on the wing suction side during strong accelerations. Surface pressure measurements confirmed that the reattachment coincided with a strong favourable pressure gradient (FPG) during acceleration. Note that for some kinematics, the reattachment of the flow prevailed long after the acceleration ended and a memory effect of the flow was observed resulting in a period of sustained lift (Marzanek & Rival 2019). Here, the term memory effect indicates the flow is still influenced significantly by events that occurred in the past (Zhou & Antonia 1995; Kriegseis, Kinzel & Rival 2013; Mamba & Magniez 2018).

With regards to non-fixed separation lines, the 6:1 major–minor ratio prolate spheroid has been a widely used benchmark model under steady conditions (Wetzel 1996; Wetzel, Simpson & Chesnakas 1998; Surana *et al.* 2006; Wu *et al.* 2007). Similar to the flow over a delta wing, on an inclined prolate spheroid, a pair of counter-rotating primary vortices originate from separation lines. The separation can be explained by the existence of strong circumferential pressure gradients (Han & Patel 1979; Tobak & Peake 1982), which is caused by the prolate spheroid surface curvature. The location of the separation lines influences the size of the wake and, therefore, significantly impacts the hydrodynamic loads. In steady conditions, the locations are attributed to the incidence angle ($\alpha$), *Re* and

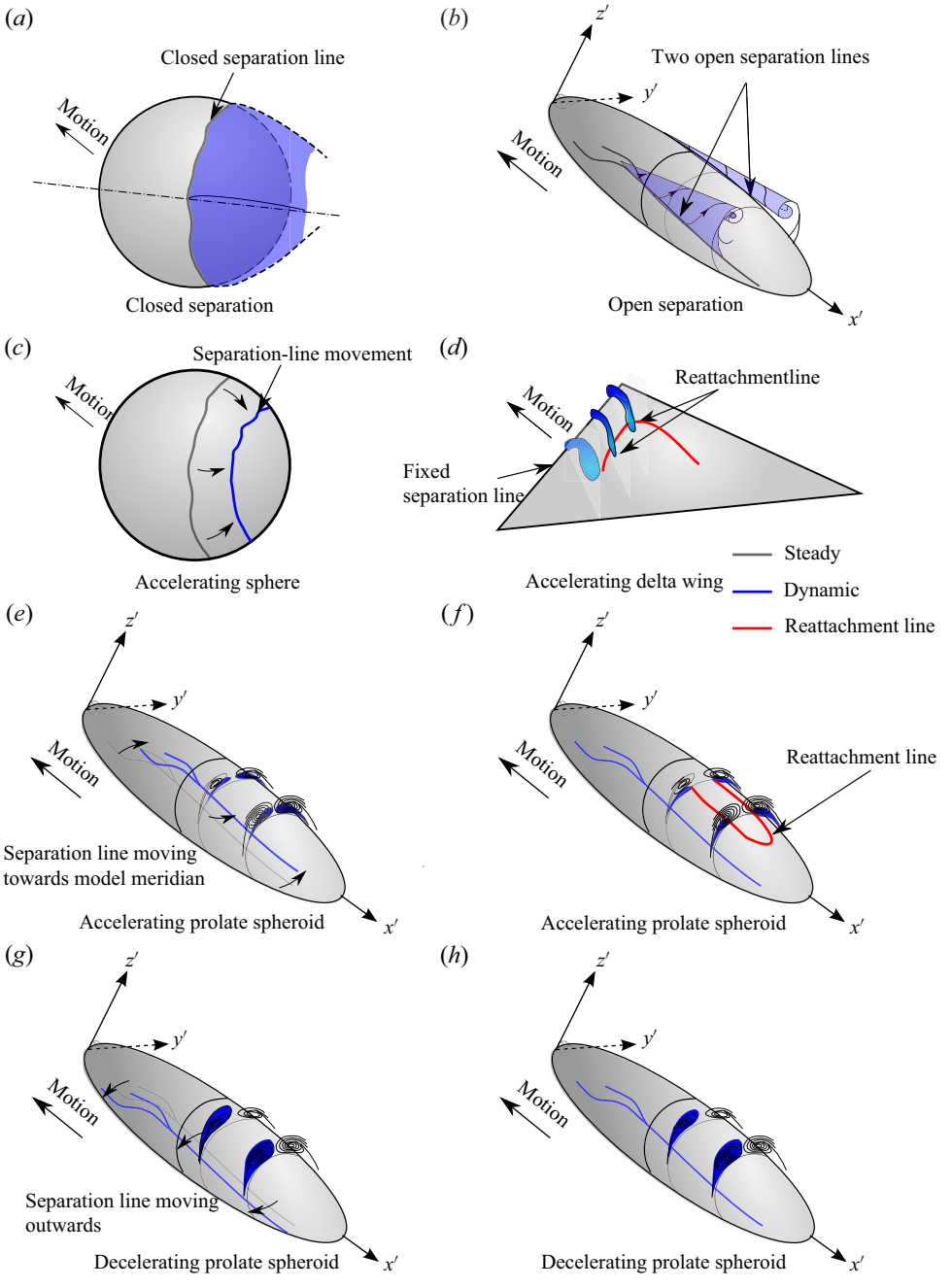


Figure 1. (*a*) Example of a closed separation with closed separation line. (*b*) A case with open separation with two open separation lines. (*c*) For an accelerating sphere, the separation line moves backwards in the subcritical *Re* range (Fernando *et al.* 2017). (*d*) For an accelerating delta wing, the flow has been observed to reattach on the wing surface (Marzanek & Rival 2019). In contrast, for an accelerating prolate spheroid, a number of scenarios are possible: (*e*) the separation line will move closer to the model meridian centre or (*f*) a reattachment line will be created. Sketches in panels (*g*) and (*h*) illustrate possible scenarios for decelerations. To make the panels clear, the possible larger cross-flow separation for decelerations is only presented on one side of the model body.

the local body radius (Jeans & Holloway 2010; Lee 2018). For unsteady conditions, Wetzel (1996) conducted measurements on a pitching prolate spheroid. The circumferential skin friction distributions on the model surface were measured via hot film sensors and the locations of minimum skin friction were used to define the separation lines. Movement of the separation lines in a circumferential direction was observed during the pitching manoeuvre, especially at higher incidence angles. However, due to the limitations in the measurements, the dynamic cross-flow patterns have not been presented.

### 1.3. *Objectives*

For the case of an inclined prolate spheroid, it remains unclear how the separated flow will vary during acceleration. In particular, the location of the separation line and the vorticity distribution in the cross-flow are likely to be affected by model acceleration and deceleration, as illustrated in figure 1(*e–h*). Similar to the aforementioned studies of spheres and delta wings, it can be expected that an FPG will form in the rear section of an inclined prolate spheroid during strong accelerations. Thus, it is hypothesized that the separation line will move closer to the model meridian; see figure 1(*e*). Similar to the dynamic flow on a delta wing, a strong FPG could mitigate the cross-flow structures and even lead to local reattachment near the model meridian; see figure 1(*f*). In contrast, for a decelerating prolate spheroid, the separation line could either move outwards (figure 1*g*) or persist at its original location as the steady condition (figure 1*h*), both resulting in larger cross-flow structures due to an increased APG during deceleration. However, it remains to be seen which of the possible flow features will occur, and how the interplay of vortical structures and surface pressure distribution will affect the separation and reattachment processes.

In addition to the initial response of the cross-flow to an acceleration, the resulting evolution of the separated structures is also of interest. Kriegseis *et al.* (2013) observed minimal memory effects from the initial attached boundary-layer vorticity to the subsequent vortex formation process on an accelerating plate. However, leading-edge vortex (LEV) formation, followed by the later shedding of the LEV, has led to an unsteady flow condition up to 14 chord lengths after acceleration (Mancini *et al.* 2015). While the exact formation time, vorticity strength and vortex stability for the LEV are dependent on plate kinematics, other studies confirmed the existence of memory effects on accelerating plates (Onoue & Breuer 2016; Kaiser, Kriegseis & Rival 2020). As discussed earlier, a different type of memory effect was observed on a non-slender delta wing. Marzanek & Rival (2019) reported a reattachment of the separated flow, which persisted even after the acceleration was completed. With regards to the inclined, accelerated prolate spheroid investigated in the present study, it is hypothesized that the separated cross-flow will also be altered for a certain distance travelled before recovery to the fully separated state. However, as the separation is open and dominated by a strong helical vortex, we expect a rapid recovery of the separated region compared with that of a (statistically) steady flow.

Therefore, the objectives of the current study are two-fold. First, we strive to understand the dynamic separation mechanics of the 3-D flow on a prolate spheroid under axial accelerations and decelerations, by capturing the separation lines and the cross-flow patterns. Furthermore, the memory effects resulting from the dynamic motions will be investigated. The present study is organized as follows. The experimental methods and model kinematics are first presented in § 2. The results of instantaneous pressure distributions, dynamic flow separation and circulation histories are then presented and

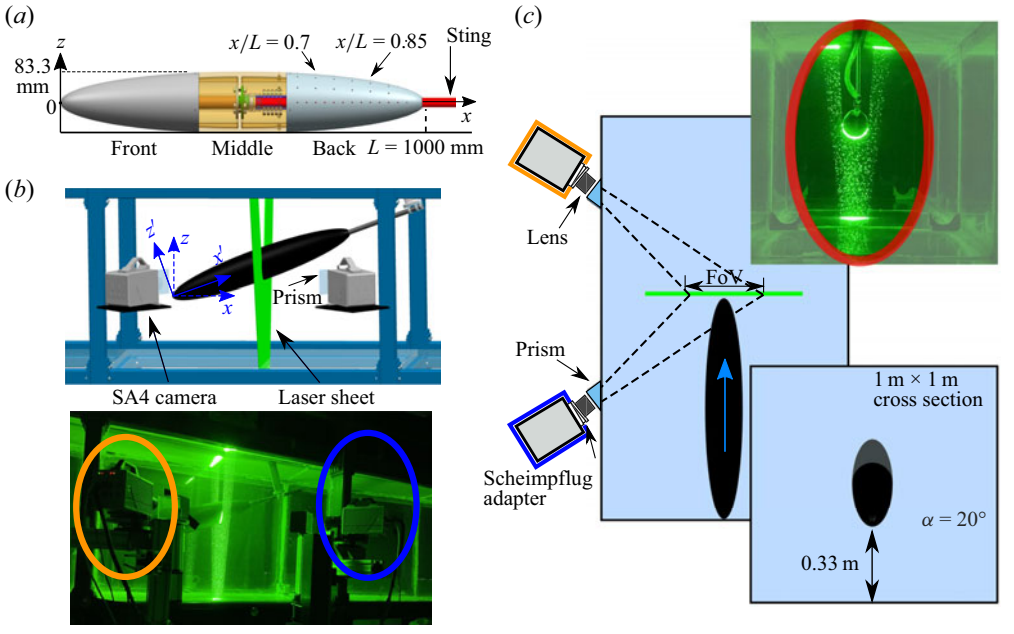


Figure 2. (*a*) Schematic of a 1-m-long 6:1 prolate-spheroid model and picture of the model; (*b*) side view of the time-resolved stereoscopic particle image velocimetry (sPIV) camera set-up consisting of two Photron SA4 cameras; and (*c*) top view of the set-up showing the moving prolate spheroid passing through the stationary laser sheet.

discussed in § 3. Finally, conclusions and practical implications of the current study are summarized in § 4.

## 2. Experimental methods

A description of the prolate-spheroid model and the experimental methods are presented in § 2.1. Thereafter, a detailed description of the model kinematics is provided in § 2.2.

### 2.1. *Experimental set-up*

All experiments were performed in a 15-m-long towing tank with a 1 m × 1 m cross-section. Three sides of the tank allow for optical access through glass panels and the top of the tank is equipped with a slotted ceiling to allow for the connection between a high-speed traverse above the tank and the model while minimizing free-surface effects. Figure 2(*a*) presents the 6:1 prolate spheroid model with length $L = 1000$ mm and the maximum diameter of $D = 166.7$ mm. The model was printed using acrylonitrile butadiene styrene (ABS), and subsequently sanded, treated with several layers of epoxy and then finished with two layers of flat-black paint to ensure a smooth surface with low reflectivity. A rear-mounted cylindrical sting connected the model to a high-speed traverse located above the tank. The model was towed at three incidence angles $\alpha \in \{10°, 15°, 20°\}$, leading to a maximum blockage ratio of 4.9 % at $\alpha = 20°$. Thus, blockage effects are considered to be negligible here.

Multiple pressure ports each with a diameter of 1.6 mm are located in the back half of the model. The pressure ports are spaced $0.05L$ in the longitudinal direction and located between $x/L = 0.6$ and $x/L = 0.95$. Along the circumferential direction, the ports are

placed at $\theta \in \{0^\circ, 30^\circ, 60^\circ, 90^\circ\}$ with $\theta = 0^\circ$ being the top (meridian centre) of the model. Owing to the symmetry of the body, only some of the pressure ports were used in the current study. Among the various sensors, eight Omega PX419 absolute pressure sensors were used. These sensors have a range of 6.89 kPa and an overall uncertainty of 0.08 % of full scale. The pressure data were acquired at a frequency of 1 kHz using a National Instruments USB-6212 DAQ system. The pressure data were normalized, leading to the pressure coefficient

$$C_p = \frac{p - p_\infty}{0.5\rho U_{II}^2}, \tag{2.1}$$

where $p$ is the instantaneous pressure measured at the pressure tap when the model is moving and the reference pressure $p_\infty$ is the static pressure far away from the body. The term $0.5\rho U_{II}^2$ is the dynamic pressure defined by the constant post-acceleration velocity $U_{II}$. The overall sensor uncertainty corresponds to an expected measurement error of $\pm 0.005 C_p$. The pressure data were ensemble-averaged over ten distinct runs.

To quantify the development of the cross-flow separation, we used a time-resolved stereoscopic particle image velocimetry (sPIV) system. Laser sheet and cameras were fixed, while the model was towed through thus allowing for a scanning reconstruction; see the work of Bond *et al.* (2019). Figure 2(*b*,*c*) shows a schematic of the sPIV set-up. The water was seeded with 60-μm polyamide particles. The flow field was illuminated with an approximately 1.5-mm-thick laser sheet generated via a 40-mJ-per-pulse Photonics Nd-YLF high-speed laser through a series of cylindrical lenses. The imaging system consisted of two Photron Fastcam SA4 cameras (1024 × 1024 pixels), each equipped with a 60-mm Nikkor lens and Scheimpflug adapters to ensure a sharp image for the entire measurement plane. A photoelectric sensor (CY-122B-P) was mounted to the towing tank and was used to trigger the recording of the sPIV system on half a model length before the acceleration. As such, synchronization between model kinematics and recording was ensured, and the acquired velocity fields were ensemble averaged. The sPIV system was operated at a frequency of 2000 Hz. Water-filled prisms were mounted on the tank to eliminate optical distortions as the cameras were installed at a slanted angle to the tank wall (Prasad & Jensen 1995; Raffel *et al.* 1998; Van Doorne & Westerweel 2007). The field of view (FoV), as labelled in figure 2(*c*), was approximately $2D \times 1.5D$ in size for all experiments. In the stereoscopic calibration procedure, a two-sided multi-plane calibration target featuring a regular grid of markers was used. The self-calibration method in DaVis 8.4.0 was employed to correct for possible misalignment between the calibration plate and the laser light sheet. A multi-pass cross-correlation algorithm and fixed final interrogation window size of 32 × 32, with 50 % overlap, was used in post-processing (Soria 1996). The particle image diameters were, on average, approximately 3 pixels. The spatial resolution of in-plane vectors was fixed at 3.6 mm. Every second recorded frame was dropped to ensure sufficient particle displacements in the cross-correlation step. The final out-of-plane displacement between correlated frames was in the range of 1–1.5 mm, corresponding to $3 \text{ px} < \delta_{px} < 6 \text{ px}$. Assuming a correlation accuracy of $\epsilon_{ip} = 0.1$ px (Raffel *et al.* 1998) for the in-plane displacement, an in-plane velocity estimation error in the range of $1.7\,\% < e_{ip} = \epsilon_{ip}/\delta_{px} < 3.3\,\%$ is expected for the present camera set-up. According to the work of Lawson & Wu (1997), the out-of-plane velocity error is approximately $2\,\% < e_{op} < 3.9\,\%$. The velocity fields were then ensemble-averaged over 20 runs to further improve the measurement accuracy.

### 2.2. *Kinematics*

An *Re* range was selected where the observed flow structures remain similar (Guo, Kaiser & Rival 2023). Weak *Re* scaling was observed for steady flow in the range of $1.0 \times 10^6 \leq Re \leq 1.5 \times 10^6$. The separation line locations as well as the vorticity distribution were observed to be very similar in this *Re* range. Therefore, in the present study, the model was accelerated from the initial velocity $U_I = 1.0\ \mathrm{m\ s^{-1}}$ ($Re = 1.0 \times 10^6$) to the final constant velocity $U_{II} = 1.5\ \mathrm{m\ s^{-1}}$ ($Re = 1.5 \times 10^6$). In contrast, the model was decelerated from $U_{II} = 1.5\ \mathrm{m\ s^{-1}}$ to $U_I = 1.0\ \mathrm{m\ s^{-1}}$, so as to ensure a range of $1.0 \times 10^6 \leq Re \leq 1.5 \times 10^6$ for both dynamic motions. The acceleration modulus is defined as

$$a^* = \frac{a_s L}{(U_{II} - U_I)^2}, \tag{2.2}$$

where $a_s$ is the physical acceleration. In the current study, the three acceleration moduli are $a^* \in \{2, 4, 6\}$, and the three deceleration moduli are $a^* \in \{-2, -4, -6\}$, all tested at three incidence angles $\alpha \in \{10^\circ, 15^\circ, 20^\circ\}$. An alternative metric to characterize the unsteadiness of the problem is the reduced frequency:

$$k = \frac{\pi f D}{U_{II}}, \tag{2.3}$$

where $f = 1/T$ is the imposed frequency and $T$ is the acceleration period. The three reduced frequencies $k \in \{0.35, 0.7, 1\}$ correspond to the three accelerations $a^* \in \{2, 4, 6\}$.

### 2.3. *Scanning PIV for unsteady flows*

Capturing an unsteady flow with a stationary time-resolved scanning sPIV system requires special attention as the model is accelerating while moving through the high-speed laser sheet. As such, the measurement section relative to the model and the time instance that is captured change simultaneously. As mentioned above, every second frame was dropped during the sPIV correlation to ensure sufficient particle displacement, leading to a time step of $\Delta t = 0.001$ s. The model displacement between two consecutive frames was $\Delta x_{max} \approx 1.5$ mm and the velocity change of the model was $\Delta U \leq 0.15\,\% U_{II}$. Therefore, the distortion of the acquired velocity fields due to the ratio of data acquisition and flow time scales is small.

To allow for a more complete analysis of the unsteady 3-D flow, the same kinematics were repeated multiple times with different physical starting positions of the model in the towing tank. As the laser sheet location was fixed, starting the acceleration earlier or later allowed one to capture a different stage of the dynamic process via the sPIV set-up, as explained by Bond *et al.* (2019). In figure 3, the instantaneous velocity ($U_{inst}$) is plotted against the dimensionless distance ($x/L$) for $a^* = 6$ and $a^* = -6$. Three different acceleration end positions are selected such that the acceleration ends when the laser sheet hits the model at $x/L = 0.5$ ($A_{0.5L}$), $x/L = 0.75$ ($A_{0.75L}$) and $x/L = 1.0$ ($A_{1.0L}$). The sPIV data were always evaluated for the rear section of the model ($0.6 \leq x/L \leq 1.0$), as the flow separation in this region was of the highest interest.

To further clarify the details of the measurements, a 3-D perspective of the model at $\alpha = 20^\circ$ is depicted in figure 3(*b*). In the body-fixed coordinate system, the three cases $A_{1.0L}$, $A_{0.75L}$ and $A_{0.5L}$ are highlighted. Specifically, the $A_{1.0L}$ case indicates that when the rear section of the model passes through the laser sheet, the model begins accelerating and the early evolution of the dynamic flow structures is captured. The $A_{0.75L}$ case represents the acceleration starting earlier and thus the flow captured here is shortly

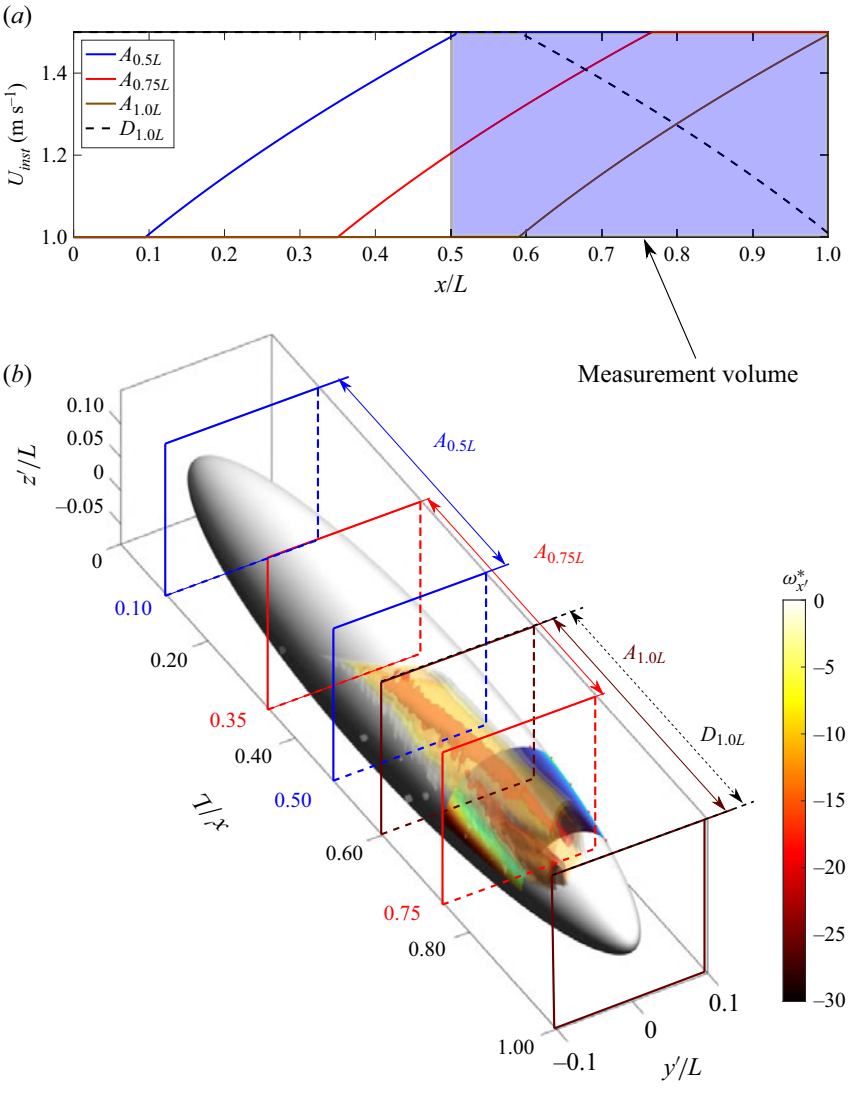


Figure 3. (*a*) Instantaneous velocity $U_{inst}$ plotted against the dimensionless distance travelled ($s^*$) for the largest acceleration modulus $a^* = 6$ and the largest deceleration modulus $a^* = -6$. (*b*) 3-D schematic showing model acceleration relative to the measurement volume.

after the acceleration. For the $A_{0.5L}$ case, the flow structures were already influenced by the acceleration over a significant amount of time (around half of the model length) and the acceleration ended before data acquisition in this rear region of the model began. The three different measurement volumes thus allow us to examine how quickly the flow reacts to the model acceleration and how quickly the cross-flow separation recovers to a stationary flow, i.e. to quantify the so-called memory effects.

## 3. Results and discussion

Here we explore the interplay between surface-pressure distribution and cross-flow evolution during rapid axial accelerations and decelerations. In particular, the influence

of the acceleration strength ($a^*$) and the (constant) incidence angle ($\alpha$) are investigated. First, the temporal evolution of the ensemble-averaged surface pressure distributions is presented in § 3.1. The impact on the streamwise and spanwise pressure gradients is then discussed in § 3.2. The interplay between the surface pressure and its effects on the cross-flow separation are then addressed in § 3.3. In particular, the location of the separation line, the streamwise vorticity field and the momentum deficit within the helical vortex structures are discussed. The variations in acceleration starting and end points relative to the laser-sheet location ($A_{0.5L}$, $A_{0.75L}$, $A_{1.0L}$) allow us to analyse how quickly the footprint of the dynamic surface pressures is observed in the vorticity fields and, in turn, how quickly the flow returns to steady state post acceleration. Finally, the evolution of the wake circulation is explored to further analyse the dynamics of cross-flow separation process.

### 3.1. *Surface pressure*

The work of Fairlie (1980) concluded that the pressure gradient and surface curvature are two driving forces to form the 3-D flow separation around a prolate spheroid. With regards to the influences from pressure gradient, Wetzel *et al.* (1998) further pointed out that the circumferential pressure gradients dominate the separation process. The present section analyses the surface pressure distribution and, in particular, its sensitivity towards axial accelerations and decelerations.

The dynamic pressure response to the rapid model acceleration has been captured for $0.7 \leq x/L \leq 0.85$ and for $0^\circ \leq \theta \leq 90^\circ$. Figure 4(*a*,*b*) present the evolution of $C_p$ at $x/L = 0.7$, $\theta = 0^\circ$ for different $a^*$ and at $\alpha = 10^\circ$ as a function of normalized time, which is defined as

$$t^* = \frac{|a_s|t}{|U_{II} - U_I|}, \tag{3.1}$$

where $t^* = 0$ and $t^* = 1$ indicate the start and end of the acceleration, respectively. With the onset of acceleration, the pressure shown in figure 4(*a*) ramps up quickly to the maximum $C_p$ ($C_p^{max}$, highlighted by orange markers) at $t^*_{max}$. The magnitude of $C_p^{max}$ is proportional to $a^*$. After the initial peak, for the smallest acceleration $a^* = 2$ in the current testing conditions, $C_p$ plateaus to an observable constant value during acceleration. The end of the acceleration is then followed by a $C_p$ minimum for all $a^*$. For the decelerating cases, the trends are inverted with $C_p$ reaching a minimum ($C_p^{min}$) shortly after the start of the deceleration at $t^*_{min}$; see figure 4(*b*).

In figure 4(*c–e*), the surface-pressure maps for the steady motion are compared with the pressure distributions at $t^*_{max}$ (acceleration) and $t^*_{min}$ (deceleration) for $|a^*| = 6$. The complete temporal evolution of acceleration ($a^* = 6$) and deceleration ($a^* = -6$) can be seen in the supplementary movies (see supplementary Movies 1 and 2 available at https://doi.org/10.1017/jfm.2023.907). Each column corresponds to one incidence angle ($\alpha = 10^\circ$, $15^\circ$ and $20^\circ$). The results for the steady condition with $Re = 1.5 \times 10^6$ are first presented in figure 4(*c*). Although all $C_p$ values are relatively small, a circumferential pressure gradient is observable acting as the footprint of the cross-flow separation process. The circumferential pressure gradient is most significant at $\alpha = 20^\circ$, corresponding to the strongest cross-flow separation driven both by streamwise APG and circumferential APG. For the accelerating case in figure 4(*d*), the $C_p$ values increase significantly in comparison to the steady condition. More importantly, for all $\alpha$, a strong streamwise FPG has been created in the longitudinal direction. This observation is in good agreement with

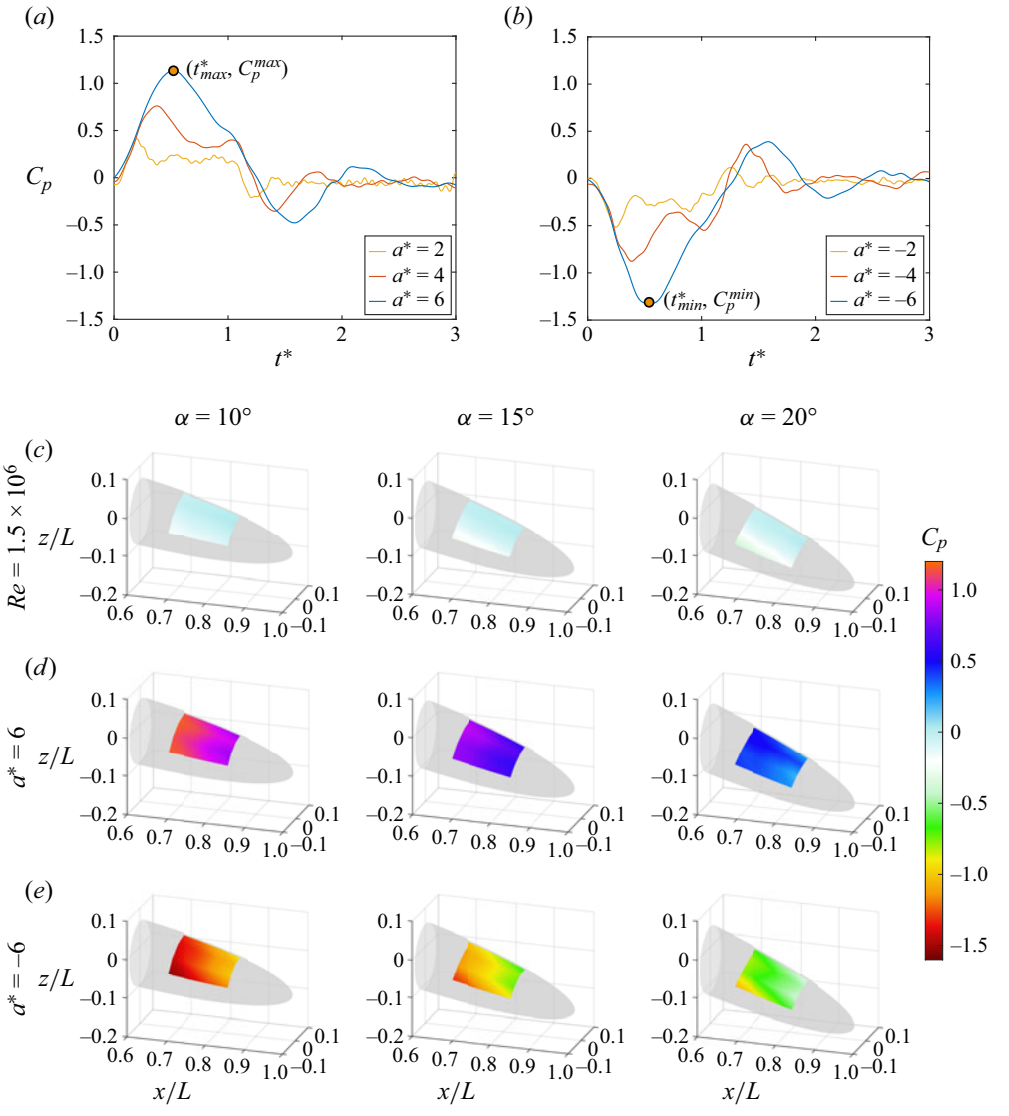


Figure 4. Ensemble-averaged pressure trends as a function of $a^*$ and $\alpha$: (*a*,*b*) time evolution of the instantaneous pressure $C_p$ for a reference point ($x/L = 0.7$, $\theta = 0°$) at $\alpha = 10°$ for various $a^*$; (*c*) steady surface pressure maps for $Re = 1.5 \times 10^6$; (*d*) surface pressure maps at time $t^*_{max}$ for $a^* = 6$; and (*e*) surface pressure maps at time $t^*_{min}$ for $a^* = -6$. The incidence angle is indicated on the top of each column. Flow is from left to right.

theoretical approximations from the potential flow field around an accelerating sphere (Fernando *et al.* 2017). However, the significant flow separation on the back half of the prolate spheroid model influences the dynamics of the pressure coefficient ($C_p$) as well. Therefore, the acceleration magnitude and incidence angle have a direct impact on $C_p$. For the same acceleration ($a^* = 6$), increasing $\alpha$ leads to a relative decrease of $C_p$. Larger $\alpha$ increases the size of the separated flow region and, thereby, decrease the influence of the acceleration on $C_p$. Furthermore, the circumferential pressure gradient, which is dominated under steady conditions, does not persist during the acceleration.

This significant change in the pressure distribution is likely to lead to a movement of the separation line and to a change of the separated cross-flow wake (strong FPG).

The surface pressure distributions during deceleration are shown in figure 4(*e*) and opposite trends relative to the acceleration case were observed. A strong APG in the streamwise direction was established and the APG in the circumferential direction was increased.

### 3.2. *Pressure gradients*

The qualitative observations presented in § 3.1 are further quantified in this section, and the scaling of the pressure gradients is compared for different values of $\alpha$ and $a^*$. We define two coefficients of streamwise and circumferential pressure gradients respectively as

$$\frac{\partial C_p}{\partial S_x} = \frac{C_p(p_{x/L=0.85}) - C_p(p_{x/L=0.7})}{dS_x/L} \tag{3.2}$$

and

$$\frac{\partial C_p}{\partial S_\theta} = \frac{C_p(p_{\theta=0^\circ}) - C_p(p_{\theta=90^\circ})}{dS_\theta/L}, \tag{3.3}$$

where $dS_x$ is the distance between two sensors along the longitudinal direction and $dS_\theta$ is the local circumferential distance at each cross-section. A higher absolute value of the coefficient indicates a stronger APG or FPG. The resulting pressure gradients are presented in figure 5. The black solid curve represents the steady condition of $Re = 1.5 \times 10^6$ (used as a reference), the solid coloured lines depict accelerations and the dashed coloured curves present the pressure gradients during decelerations.

In figure 5(*a–c*), the streamwise pressure gradient ($\partial C_p/\partial S_x$) is shown for various $\theta$ positions. For all $\theta$, acceleration causes the pressure-gradient field to be transformed from APG to FPG. Furthermore, the strength of the streamwise FPG is increased with increasing $a^*$, which is in good agreement with the theoretical predictions based on potential theory for an accelerating sphere (Fernando *et al.* 2017) and for an accelerating flat plate at incidence (Guo *et al.* 2021), where the strength of the FPG was shown to be linearly dependent on the acceleration magnitude. In contrast, the pressure-gradient field is still covered by the streamwise APG for all decelerations and the strength of the APG increases also with increasing deceleration magnitude.

The distribution of $\partial C_p/\partial S_\theta$ at $x/L \in \{0.70, 0.75, 0.80, 0.85\}$ is presented in figure 5(*d–f*). For $Re = 1.5 \times 10^6$, the circumferential APG strength increases from $\alpha = 10^\circ$ to $\alpha = 20^\circ$ due to the stronger cross-flow at a higher $\alpha$. As observed in § 3.1, the circumferential pressure gradient ($\partial C_p/\partial S_\theta$) is significantly reduced during acceleration. For $a^* = 6$ at $x/L = 0.85$, we even observe a weak circumferential FPG for all $\alpha$. While $\partial C_p/\partial S_\theta$ strongly depends on $\alpha$ for the steady reference case, the acceleration reduces $\partial C_p/\partial S_\theta$ to very small magnitudes, regardless of $\alpha$ or $a^*$. In contrast, the $\partial C_p/\partial S_\theta$ is further increased during decelerations, leading to strong circumferential APGs. The magnitude of $\partial C_p/\partial S_\theta$ is more affected by the deceleration for $\alpha = 10^\circ$ than for the $\alpha = 20^\circ$ case (compare figure 5*d–f*), where a large cross-flow separation already exists in the steady state.

Summarizing §§ 3.1 and 3.2, we conclude that the pressure-gradient field around an accelerating or decelerating spheroid is strongly influenced through axial acceleration. Not only is the magnitude of the pressure gradients influenced but furthermore, the gradient flips from APG to FPG in streamwise and circumferential directions. Therefore, we expect changes in the formation and subsequent evolution of the cross-flow structures as well.

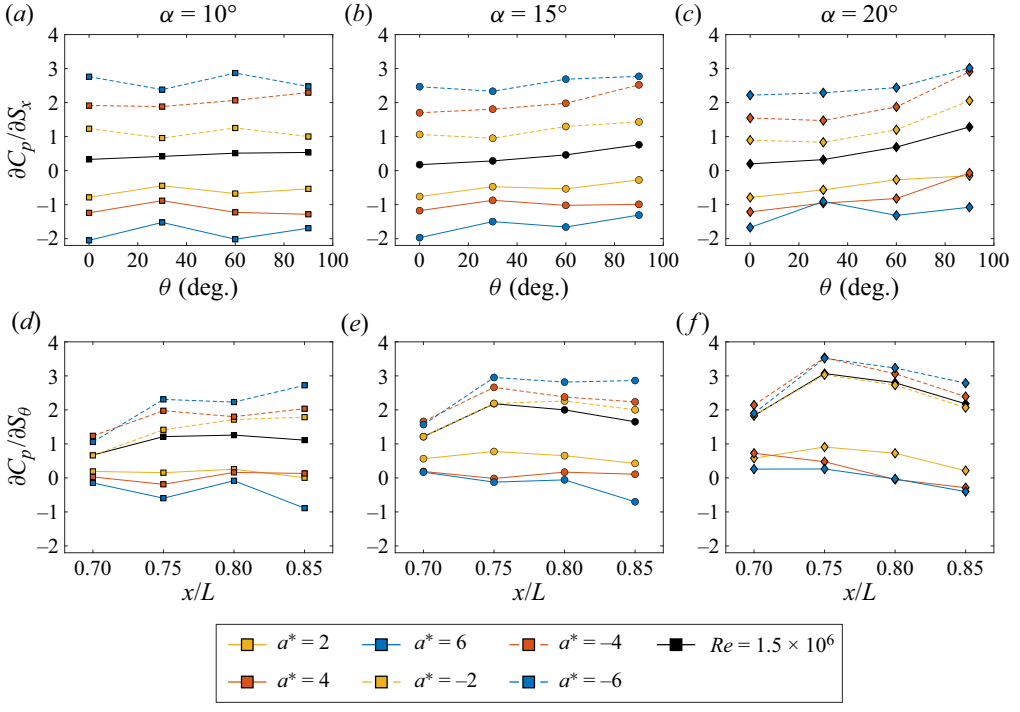


Figure 5. Trends in pressure gradients as a function of acceleration/deceleration magnitudes $a^*$ and incidence angle $\alpha$: (*a–c*) for streamwise pressure gradient coefficient and (*d–f*) for spanwise pressure gradient coefficient. The incidence angle ($\alpha$) is indicated on the top of each column.

### 3.3. *Streamwise vorticity and velocity distributions*

After observing the significant influence of the acceleration in § 3.2, we now discuss how the streamwise vorticity and velocity are influenced by acceleration. Here vorticity and velocity are normalized by the local instantaneous velocity ($U_{inst}$) on each cross-section. The normalized (axial) vorticity is defined as

$$\omega_x^* = \frac{\omega_x L}{U_{inst}}. \tag{3.4}$$

Figure 6 presents the streamwise vorticity in the lab-fixed frame of reference and that $u = U_{inst}$ would indicate that the fluid is moving at the same speed as the model. For sake of brevity, only the most extreme cases with largest acceleration ($a^* = 6$) and deceleration ($a^* = -6$), at incidence angle $\alpha = 20^\circ$, are shown in figure 6 and discussed in detail. For each case, three cross-sections ($x/L \in \{0.65, 0.85, 0.9\}$; see figure 3) are examined to present the streamwise vorticity ($\omega_x^*$) and streamwise velocity ($u/U_{inst}$). The supplementary movie (see Movie 3) displays the complete evolution of vorticity on the rear section ($0.65 \leq x/L \leq 0.90$). In figure 6, an orange diamond highlights the azimuthal position, where a significant deviation from the free-stream velocity is captured close to the model's surface. The orange diamond provides a visual indication for the extent of the cross-flow separation.

Figure 6(*a–c*) presents results for the steady case as a reference. As discussed in a related study on steady wakes (Guo *et al.* 2023), a helical vortex tube is formed at relatively small $x/L$; see figure 6(*a*). Travelling downstream, the core of the vortex tube aligns with the mean flow direction, resulting in a high-velocity region away from the

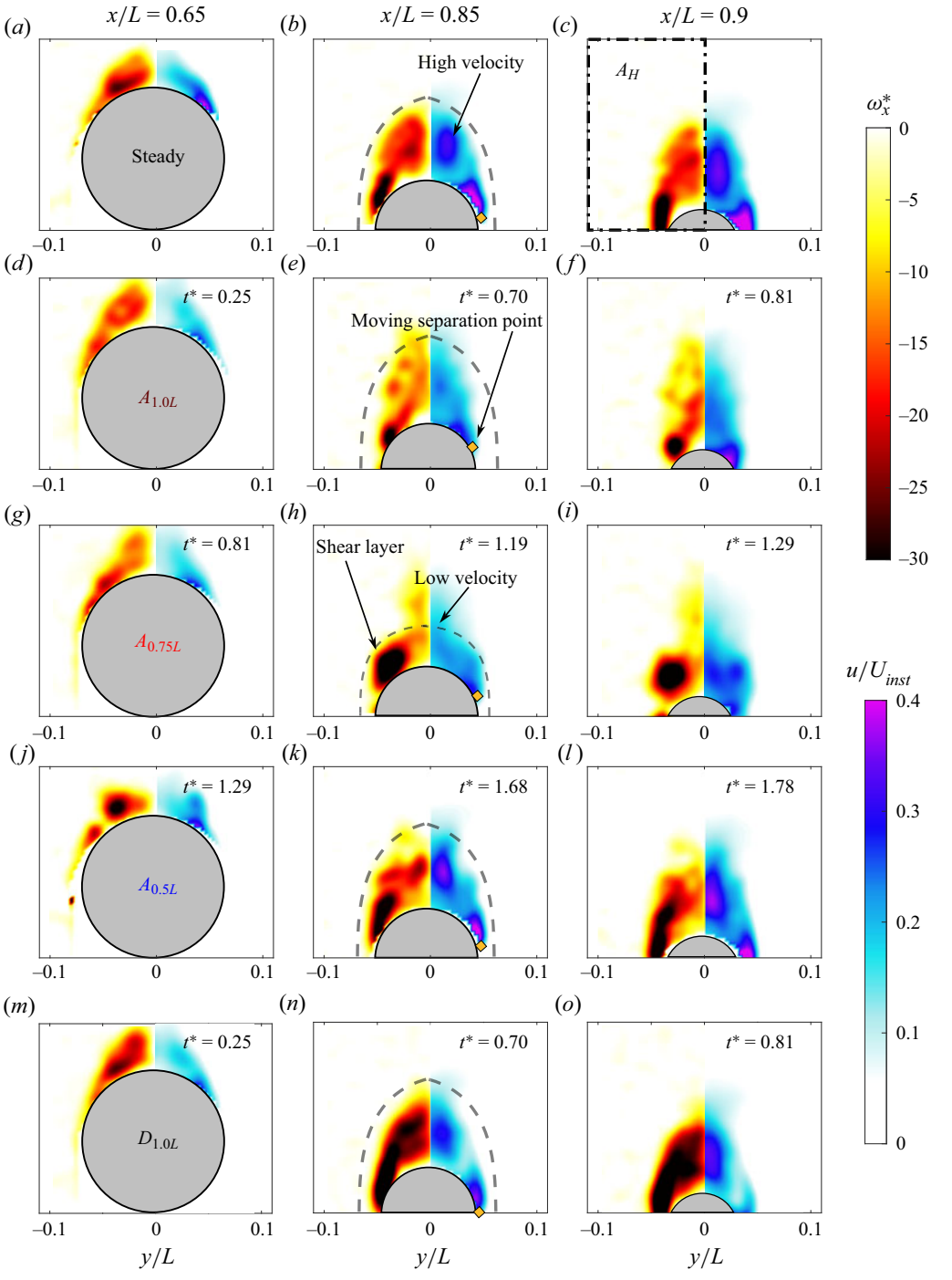


Figure 6. Streamwise vorticity and velocity for $a^* = 6$ and $a^* = -6$ at $\alpha = 20^\circ$: (*a–c*) steady $Re = 1.5 \times 10^6$; (*d–f*) $A_{1.0L}$; (*g–i*) $A_{0.75L}$; (*j–l*) $A_{0.5L}$ and (*m–o*) $D_{1.0L}$. The size of the cross-flowseparation is highlighted by the orange diamonds on the streamwise velocity distributions. In the $A_{1.0L}$ and $A_{0.75L}$ cases, the separation point moves closer to the meridian centre of the model. In contrast, acceleration has no effect on the separation point in the $A_{0.5L}$ case. The point moves outwards in the $D_{1.0L}$ case.

model, as highlighted in figure 6(*b*). To gather insights into the temporal evolution of the cross-flow during acceleration, we present cross-sections of all accelerations ($A_{1.0L}$, $A_{0.75L}$ and $A_{0.5L}$) and $t^*$ is indicated in the top right corner of each panel. Figure 6(*d–f*) shows $A_{1.0L}$ and thus the early evolution of the flow field directly after acceleration has begun. In figure 6(*d*), the flow has not yet adapted to the changing boundary conditions. However, downstream (figure 6*e*,*f*), the impact of the increased FPG is observable, and the original high-velocity region away from the model is already slightly suppressed. At the same time, the separation line has moved inwards indicating that the reduction in the circumferential APG (see § 3.2) directly impacts the location of the separation. The impact of the acceleration becomes even more apparent later on. Even though the acceleration is already complete in figure 6(*h*,*i*), most vorticity is concentrated close to the model surface and the momentum deficit in the wake is significantly reduced. As indicated by the dashed line, the helical vortex structures are closely attached to the spheroid at this time.

Figure 6(*j–l*) presents the post-acceleration evolution ($A_{0.5L}$) and highlights how quickly the flow returns to steady state. The strong FPG reduces cross-flow separation and even reattaches the 3-D separated flows (Marzanek & Rival 2019). However, in contrast with the hypothesis shown in figure 1(*d*), the flow does not fully reattach for the present kinematics. A sustained strong acceleration resulting in strong FPG at smaller incidence angles could still validate the hypothesis but goes beyond the scope of the present study. As shown in figure 6(*k*), the separation line moves outwards again at $t^* = 1.68$, and vorticity and velocity fields already look very similar as in the steady state shown in figure 6(*b*). As such, the memory effect in the present flow relative to a sudden change of boundary conditions is significantly smaller when compared to previous studies on other model geometries such as by Kaiser *et al.* (2020) and Marzanek & Rival (2019). Owing to the open separation on the elongated body of the prolate spheroid, the material volume of fluid that is directly affected by the acceleration quickly convects into the wake. In turn, the body acceleration quickly loses influence on the separated flow close to the prolate spheroid.

The $D_{1.0L}$ case in figure 6(*m–o*) exhibits stronger flow separation due to the stronger APG in both streamwise and circumferential directions. The separation point moves away from the meridian, which is consistent with the hypothesis suggested in figure 1(*e*).

### 3.4. *Circulation of streamwise vortices*

The results up to this point show that dynamic motions have a significant influence on the resulting cross-flow structures. However, changes in the dynamic loads are often of primary interest in the context of flow separation on manoeuvring bodies. Prior studies have shown that the loads are closely connected to the separation size and strength, which can be further quantified by the circulation (Fu *et al.* 1994). In the current study, the circulation was obtained by integrating the streamwise vorticity over one side of the body (area $A_H$ in figure 6*c*), such that normalized circulation can be defined as

$$\Gamma^* = \int_{A_H} \omega_x^* \, \mathrm{d}A_H. \tag{3.5}$$

In figure 7, the magnitude of $\Gamma^*$ is shown for the steady case ($Re = 1.5 \times 10^6$), $A_{1.0L}$, $A_{0.75L}$, $A_{0.5L}$ and $D_{1.0L}$ all at $\alpha = 20^\circ$. Figure 7(*a*) shows cases for acceleration $a^* = 6$ and deceleration $a^* = -6$, while figure 7(*b*) represents $a^* = 4$ and $a^* = -4$ since the streamwise FPG could be maintained for an extended period of time (see figure 4).

The separated shear layer continues to feed vorticity into the cross-flow, which leads to an increase of $\Gamma^*$ with $x/L$. Thus, an increasing $\Gamma^*$ indicates the growth process of the

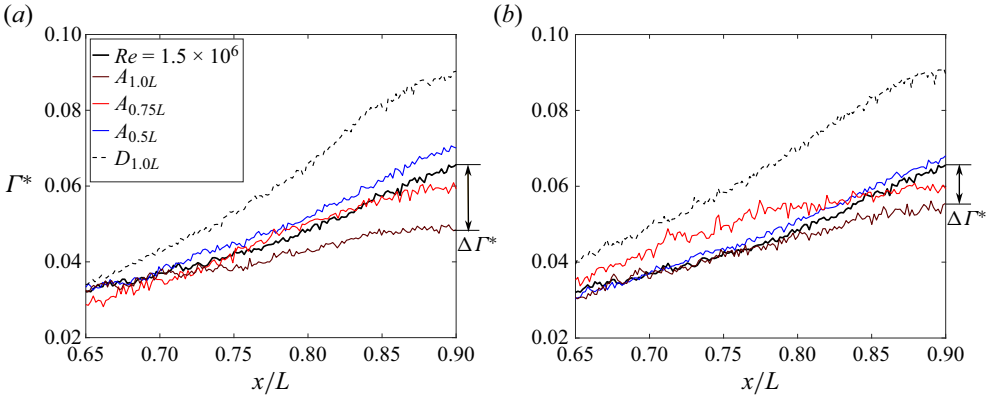


Figure 7. Circulation of streamwise vortices ($\Gamma^*$) at $\alpha = 20^\circ$ with cross-sections ($x/L$): (*a*) for $a^* = 6$ and $a^* = -6$; (*b*) for $a^* = 4$ and $a^* = -4$. Only during acceleration ($A_{1.0L}$ case), acceleration has a great influence on the circulation. In contrast, deceleration works on strengthening flow separation.

streamwise vortices along the body for all cases. The steady condition ($Re = 1.5 \times 10^6$) is again shown as a reference in both panels. Note that if the response to the acceleration were to be instantaneous (quasi-steady), all lines would collapse since $\Gamma^*$ is normalized by $U_{inst}$, see (3.4) and (3.5). However, when the $\Gamma^*$ curve lies below the steady reference line, it suggests that less vorticity is shed into the cross-flow during acceleration. Varying growth rates for $A_{1.0L}$, $A_{0.75L}$, $A_{0.5L}$ and $D_{1.0L}$ are observed, and will be discussed below to explain the effects of acceleration or deceleration on vortex formation.

We start the discussion with $A_{1.0L}$. The $\Gamma^*_{A_{1.0L}}$ curve begins to deviate from the steady reference for $x/L > 0.7$, indicating a lag in the flow to the acceleration that started at $x/L = 0.6$. In the following, the difference between $A_{1.0L}$ and the steady reference increases as highlighted by $\Delta\Gamma^*$ in figure 7(*a*). This increasing deviation shows how the helical vortices do not directly adapt to the instantaneous velocity. Consistent with the $A_{1.0L}$ result, the circulation from $A_{0.75L}$ starts with smaller values than the steady reference case but approaches the steady result later. Finally, for $A_{0.5L}$, the sPIV measurement takes place after the acceleration is completed. It is apparent that $\Gamma^*$ is quite similar to the steady curve, reconfirming the short-lived memory effect for the open cross-flow as mentioned in § 3.3. The deceleration case is represented by a dashed line in figure 7(*a*) and shows much higher normalized circulation values, indicating a stronger cross-flow separation than the steady or accelerated cases. This observation is in good agreement with the instantaneous vorticity fields shown in figure 6(*m–o*).

Finally, the evolution of $\Gamma^*$ at $a^* = 4$ and $a^* = -4$ is shown in figure 7(*b*). The same trends can be observed as in figure 7(*a*). However, the gap $\Delta\Gamma^*$ is smaller than that for $a^* = 6$. The $\Gamma^*$ curve for the $A_{0.75L}$ case is relatively high when compared with the steady result at $0.7 \leq x/L \leq 0.8$, which is attributed to the stronger shear layer, as shown in figure 6(*h*).

## 4. Conclusions

A series of experiments to investigate the dynamic separation on an accelerating and decelerating prolate spheroid have been conducted. The instantaneous surface pressure, as a function of acceleration strength ($a^*$) and incidence angle ($\alpha$), has been collected, and the 3-D flow separation about the prolate spheroid was measured using scanning sPIV,

from which the moving separation line, the streamwise momentum deficit, the streamwise vorticity and eventually the circulation have all been extracted.

The main findings in the current study are summarized as follows.

(1) The pressure gradient on the prolate spheroid responds rapidly to axial acceleration and deceleration. During acceleration, the character of the streamwise pressure gradient transforms from adverse to favourable. Furthermore, the strength of the streamwise FPG increases with increasing acceleration magnitude. This phenomenon is stronger for small $\alpha$. At the same time, the acceleration removes the circumferential pressure gradients, which are prominent during steady motion. In contrast, for a decelerating prolate spheroid, the streamwise and the circumferential adverse pressure gradients are both amplified.

(2) The separation line on the prolate spheroid surface moves as a result of the rapid change in streamwise velocity. The separation line moves closer to the model meridian centre during acceleration as a result of the vanishing circumferential APG, while moving outwards during deceleration due to a stronger APG along both streamwise and circumferential directions.

(3) In addition to the moving separation line, an axial acceleration also leads to a change of the flow structures in the separated cross-flow. The helical vortex structure remains close to the model and does not align with the mean-flow direction as is observed for the steady case. As such, a region of concentrated vorticity was observed close to the body, while the momentum deficit in the wake is reduced. In contrast, for axial deceleration, the wake remains aligned with the mean-flow direction. However, more vorticity is shed, leading to an increase in streamwise circulation.

(4) While the surface pressures react instantaneously to acceleration, the observed flow fields respond with a small delay. This lag is in good agreement with earlier studies with hysteresis in unsteady turbulent separation (Ambrogi, Piomelli & Rival 2022). Furthermore, the separation line remains at its unaltered position even shortly after the acceleration is completed, indicating a weak memory effect in the cross-flow. However, the cross-flow recovers quickly to the steady state and the separation line moves back to its original location.

Despite the insights gathered in the present manuscript, several open questions remain. For instance, would sustained accelerations at smaller incidence angles reattach the separated flow? Future work could also decouple the effects of the pressure gradient and curvature on the formation of 3-D cross-flow separation by systematically varying the model geometry.

**Supplementary movies.** Supplementary movies are available at https://doi.org/10.1017/jfm.2023.907.

**Acknowledgements.** The authors would like to thank Wenchao Yang and Dashuai Chen for assistance with the initial experimental set-up, as well as JiaCheng Hu and Adnan EI Makdah in the same research group for their fruitful input.

**Funding.** The research was supported by DER's NSERC Discovery grant.

**Declaration of interests.** The authors report no conflict of interest.

**Author ORCIDs.**
Pengming Guo https://orcid.org/0000-0002-2867-052X;
Frieder Kaiser https://orcid.org/0000-0001-9888-8770;
David E. Rival https://orcid.org/0000-0001-7561-6211.

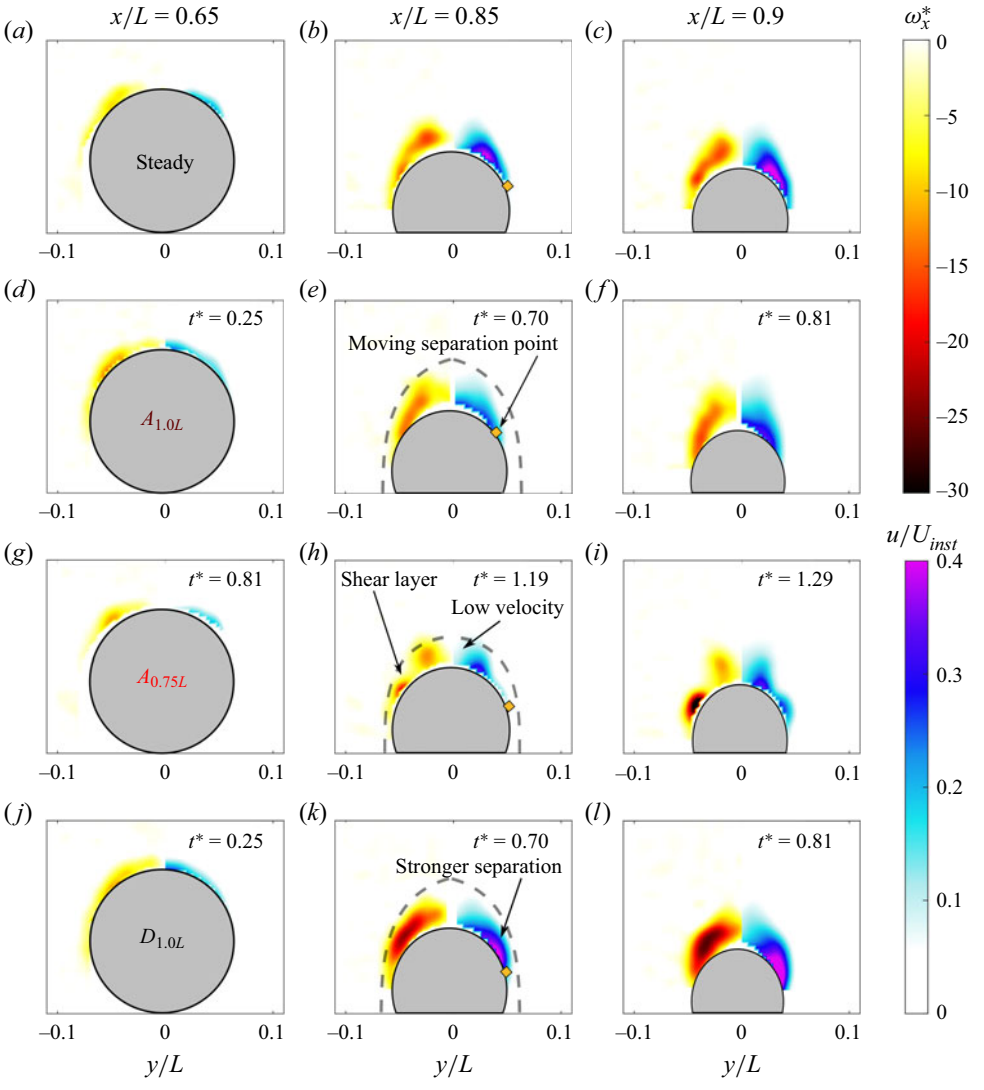


Figure 8. Streamwise vorticity and velocity for $a^* = 6$ and $a^* = -6$ at $\alpha = 10^\circ$: (*a–c*) steady $Re = 1.5 \times 10^6$; (*d–f*) $A_{1.0L}$; (*g–i*) $A_{0.5L}$ and (*j–l*) $D_{1.0L}$. The location of the separation point is marked by the orange diamonds on the streamwise velocity distributions.

**Author contributions.** All authors, conceptualization and methodology; P.G. and F.K., experimental execution, software, visualization and writing of the original draft; D.E.R., acquisition of funding, supervision, reviewing and editing.

## Appendix

The cases with the largest acceleration ($a^* = 6$) and deceleration ($a^* = -6$) at a milder incidence angle $\alpha = 10^\circ$ are compared in figure 8. Identical to figure 6, three cross-sections ($x/L \in \{0.65, 0.85, 0.9\}$) are chosen to present the streamwise vorticity ($\omega_x^*$), streamwise velocity ($u/U_{inst}$) and the trend of the moving separation point. Figure 8(*a–c*) shows steady results as a reference. Compared with the largest incidence angle $\alpha = 20^\circ$, a much smaller

cross-flow separation is observed above the model surface. For temporal evolution of the cross-flow separation during the acceleration ($A_{1.0L}$, figure 8*d–f*), the impact of the increased FPG can be observed through the suppressed high-velocity region. The inward movement of the separation line also indicates the reduction in the circumferential APG, showing the same trend as the observation in figure 6(*d–f*). When the acceleration is complete, as seen in figure 8(*g–i*), the vorticity is more concentrated and the helical vortex structures more closely adhere to the model surface, corresponding to the observation in figure 6(*h–i*). Figure 8(*j–l*) represents deceleration conditions ($D_{1.0L}$) and shows enhanced flow separation due to a stronger APG in both the streamwise and circumferential directions. The trend in the separation point movement is also consistent at the largest incidence angle $\alpha = 20°$. However, due to the small cross-flow separation, whether the separated flow re-attaches on the model surface under these current accelerations cannot be confirmed.

## References


Ambrogi, F., Piomelli, U. & Rival, D.E. 2022 Characterization of unsteady separation in a turbulent boundary layer: mean and phase-averaged flow. *J. Fluid Mech.* **945**, A10.

Bettle, M.C., Gerber, A.G. & Watt, G.D. 2009 Unsteady analysis of the six DOF motion of a buoyantly rising submarine. *Comput. Fluids* **38** (9), 1833–1849.

Bond, C., Marzanek, M.F., Neeteson, N.J. & Rival, D.E. 2019 On the volumetric reconstruction of transiting wakes using stereoscopic-PIV. *Exp. Fluids* **60** (10), 1–10.

Cheney, J.A., Stevenson, J.P.J., Durston, N.E., Song, J., Usherwood, J.R., Bomphrey, R.J. & Windsor, S.P. 2020 Bird wings act as a suspension system that rejects gusts. *Proc. R. Soc.* B **287** (1937), 20201748.

Deck, S. 2012 Recent improvements in the zonal detached eddy simulation (ZDES) formulation. *Theor. Comput. Fluid Dyn.* **26** (6), 523–550.

Délery, J.M. 2001 Robert Legendre and Henri Werlé: toward the elucidation of three-dimensional separation. *Annu. Rev. Fluid Mech.* **33** (1), 129–154.

El Khoury, G.K., Andersson, H.I. & Pettersen, B. 2012 Wakes behind a prolate spheroid in crossflow. *J. Fluid Mech.* **701**, 98–136.

Elyasi, M. & Ghaemi, S. 2019 Experimental investigation of coherent structures of a three-dimensional separated turbulent boundary layer. *J. Fluid Mech.* **859**, 1–32.

Fairlie, B.D. 1980 Flow separation on bodies of revolution at incidence. In *7th Australian Hydraulics and Fluid Mechanics Conference, Brisbane*, pp. 18–22.

Fernando, J.N., Marzanek, M., Bond, C. & Rival, D.E. 2017 On the separation mechanics of accelerating spheres. *Phys. Fluids* **29** (3), 037102.

Fu, T.C., Shekarriz, A, Katz, J. & Huang, T.T. 1994 The flow structure in the lee of an inclined 6: 1 prolate spheroid. *J. Fluid Mech.* **269**, 79–106.

Guo, P., Kaiser, F. & Rival, D.E. 2023 Vortex-wake formation and evolution on a prolate spheroid at subcritical Reynolds numbers. *Exp. Fluids* **64** (10), 167.

Guo, P., Zhang, K., Yasuda, Y., Yang, W., Galipon, J. & Rival, D.E. 2021 On the influence of biomimetic shark skin in dynamic flow separation. *Bioinspir. Biomim.* **16** (3), 034001.

Gursul, I. 2005 Review of unsteady vortex flows over slender delta wings. *J. Aircraft* **42** (2), 299–319.

Haller, G. 2004 Exact theory of unsteady separation for two-dimensional flows. *J. Fluid Mech.* **512**, 257–311.

Han, T. & Patel, V.C. 1979 Flow separation on a spheroid at incidence. *J. Fluid Mech.* **92** (4), 643–657.

Hwang, J.-Y., Yang, K.-S. & Sun, S.-H. 2003 Reduction of flow-induced forces on a circular cylinder using a detached splitter plate. *Phys. Fluids* **15** (8), 2433–2436.

Jeans, T.L. & Holloway, A.G.L. 2010 Flow-separation lines on axisymmetric bodies with tapered tails. *J. Aircraft* **47** (6), 2177–2183.

Jiang, F., Andersson, H.I., Gallardo, J.P., Okulov, V.L. 2016 On the peculiar structure of a helical wake vortex behind an inclined prolate spheroid. *J. Fluid Mech.* **801**, 1–12.

Kaiser, F., Kriegseis, J. & Rival, D.E. 2020 The influence of edge undulation on vortex formation for low-aspect-ratio propulsors. *J. Fluid Mech.* **883**, A55.

KRIEGSEIS, J., KINZEL, M. & RIVAL, D.E. 2013 On the persistence of memory: do initial conditions impact vortex formation? *J. Fluid Mech.* **736**, 91–106.

LAMARCHE-GAGNON, M.-E. & VÉTEL, J. 2018 Experimental investigation of unsteady separation in the rotor-oscillator flow. *J. Fluid Mech.* **844**, 546–566.

LAWSON, N.J. & WU, J. 1997 Three-dimensional particle image velocimetry: error analysis of stereoscopic techniques. *Meas. Sci. Technol.* **8** (8), 894.

LE, H., MOIN, P. & KIM, J. 1997 Direct numerical simulation of turbulent flow over a backward-facing step. *J. Fluid Mech.* **330**, 349–374.

LEE, S.-K. 2018 Longitudinal development of flow-separation lines on slender bodies in translation. *J. Fluid Mech.* **837**, 627–639.

LEGENDRE, R. 1952 Écoulement au voisinage de la pointe avant d'une aile à forte flèche aux incidences moyennes. *La Rech. Aéronaut.* **30**, 3–8.

LI, Z.-Y., FENG, L.-H., KISSING, J., TROPEA, C. & WANG, J.-J. 2020 Experimental investigation on the leading-edge vortex formation and detachment mechanism of a pitching and plunging plate. *J. Fluid Mech.* **901**, A17.

LIGHTHILL, M.J. 1963 2.6 attachment and separation in three-dimensional flows. Laminar boundary layers.

LOWSON, M.V. & RILEY, A.J. 1995 Vortex breakdown control by delta wing geometry. *J. Aircraft* **32** (4), 832–838.

MA, A., GIBEAU, B. & GHAEMI, S. 2020 Time-resolved topology of turbulent boundary layer separation over the trailing edge of an airfoil. *J. Fluid Mech.* **891**, A1.

MAMBA, S.S. & MAGNIEZ, J.C. 2018 Dynamics of a liquid plug in a capillary tube under cyclic forcing: memory effects and airway reopening. *J. Fluid Mech.* **838**, 165–191.

MANCINI, P., MANAR, F., GRANLUND, K., OL, M.V. & JONES, A.R. 2015 Unsteady aerodynamic characteristics of a translating rigid wing at low Reynolds number. *Phys. Fluids* **27** (12), 123102.

MARZANEK, M.F. & RIVAL, D.E. 2019 Separation mechanics of non-slender delta wings during streamwise gusts. *J. Fluids Struct.* **90**, 286–296.

MIOTTO, R., WOLF, W., GAITONDE, D. & VISBAL, M. 2022 Analysis of the onset and evolution of a dynamic stall vortex on a periodic plunging aerofoil. *J. Fluid Mech.* **938**, A24.

MITCHELL, A.M. & DÉLERY, J. 2001 Research into vortex breakdown control. *Prog. Aerosp. Sci.* **37** (4), 385–418.

MOORE, F.K. 1958 On the separation of the unsteady laminar boundary layer. In *Grenzschichtforschung/ Boundary Layer Research*, pp. 296–311. Springer.

ONOUE, K. & BREUER, K.S. 2016 Vortex formation and shedding from a cyber-physical pitching plate. *J. Fluid Mech.* **793**, 229–247.

PRANDTL, L. 1904 Über flussigkeitsbewegung bei sehr kleiner reibung. *Verhandl. III, Internat. Math.-Kong., Heidelberg, Teubner, Leipzig, 1904*, pp. 484–491.

PRASAD, A.K. & JENSEN, K. 1995 Scheimpflug stereocamera for particle image velocimetry in liquid flows. *Appl. Opt.* **34** (30), 7092–7099.

RAFFEL, M., WILLERT, C.E., KOMPENHANS, J., *et al.*1998 *Particle Image Velocimetry: A Practical Guide*, vol. 2. Springer.

ROTT, N. 1956 Unsteady viscous flow in the vicinity of a stagnation point. *Q. Appl. Maths* **13** (4), 444–451.

SEARS, W.R. & TELIONIS, D.P. 1971 Unsteady boundary-layer separation. *Recent Research on Unsteady Boundary Layers*, vol. 1, pp. 404–447. Laval University Press, Quebec.

SIMPSON, R. 1995 Three-dimensional turbulent boundary layers and separation. In *33rd Aerospace Sciences Meeting and Exhibit*, p. 226. American Institute of Aeronautics and Astronautics.

SIMPSON, R.L., CHEW, Y.-T. & SHIVAPRASAD, B.G. 1981 The structure of a separating turbulent boundary layer. Part 1. Mean flow and Reynolds stresses. *J. Fluid Mech.* **113**, 23–51.

SORIA, J. 1996 An investigation of the near wake of a circular cylinder using a video-based digital cross-correlation particle image velocimetry technique. *Exp. Therm. Fluid Sci.* **12** (2), 221–233.

STEVENSON, J.P.J., NOLAN, K.P. & WALSH, E.J. 2016 Particle image velocimetry measurements of induced separation at the leading edge of a plate. *J. Fluid Mech.* **804**, 278–297.

SURANA, A., GRUNBERG, O. & HALLER, G. 2006 Exact theory of three-dimensional flow separation. Part 1. Steady separation. *J. Fluid Mech.* **564**, 57–103.

TOBAK, M. & PEAKE, D.J. 1982 Topology of three-dimensional separated flows. *Annu. Rev. Fluid Mech.* **14** (1), 61–85.

VAN DOORNE, C.W.H. & WESTERWEEL, J. 2007 Measurement of laminar, transitional and turbulent pipe flow using stereoscopic-PIV. *Exp. Fluids* **42** (2), 259–279.

WANG, K.C. 1972 Separation patterns of boundary layer over an inclined body of revolution. *AIAA J.* **10** (8), 1044–1050.

WANG, K.C. 1974 Boundary layer over a blunt body at high incidence with an open-type of separation. *Proc. R. Soc. Lond.* A *Math. Phys. Sci.* **340** (1620), 33–55.

WANG, K.C. 1976 Separation of three-dimensional flow. *Reviews in Viscous Flow*, pp. 341–414. Lockheed-Georgia Co Symposium LG 77 ER 0044.

WETZEL, T.G. 1996 *Unsteady Flow Over a 6:1 Prolate Spheroid*. Virginia Polytechnic Institute and State University.

WETZEL, T.G., SIMPSON, R.L. & CHESNAKAS, C.J. 1998 Measurement of three-dimensional crossflow separation. *AIAA J.* **36** (4), 557–564.

WU, J.-Z., MA, H.-Y. & ZHOU, M.-D. 2007 *Vorticity and Vortex Dynamics*. Springer Science & Business Media.

WU, J.Z., TRAMEL, R.W., ZHU, F.L. & YIN, X.Y. 2000 A vorticity dynamics theory of three-dimensional flow separation. *Phys. Fluids* **12** (8), 1932–1954.

YU, Y., AMANDOLESE, X., FAN, C. & LIU, Y. 2018 Experimental study and modelling of unsteady aerodynamic forces and moment on flat plate in high amplitude pitch ramp motion. *J. Fluid Mech.* **846**, 82–120.

ZHANG, D., HUANG, Q.-G., PAN, G., YANG, L.-M. & HUANG, W.-X. 2022 Vortex dynamics and hydrodynamic performance enhancement mechanism in batoid fish oscillatory swimming. *J. Fluid Mech.* **930**, A28.

ZHOU, Y. & ANTONIA, R.A. 1995 Memory effects in a turbulent plane wake. *Exp. Fluids* **19** (2), 112–120.